

## RESEARCH ARTICLE

10.1029/2020JB020401

## Key Points:

- Spectral element simulation can be used to calculate gravitoelastic correlations of ambient seismic fields
- Topography at Sardinian candidate site of Einstein Telescope has significant impact on gravitoelastic correlations
- Topography at Sardinian site acts as low-pass filter for Rayleigh waves

## Correspondence to:

T. Andric,  
tomislav.andric@gssi.it

## Citation:

Andric, T., & Harms, J. (2020). Simulations of gravitoelastic correlations for the Sardinian candidate site of the Einstein Telescope. *Journal of Geophysical Research: Solid Earth*, 125, e2020JB020401. <https://doi.org/10.1029/2020JB020401>

Received 17 JUN 2020

Accepted 23 SEP 2020

Accepted article online 28 SEP 2020

## Simulations of Gravitoelastic Correlations for the Sardinian Candidate Site of the Einstein Telescope

Tomislav Andric<sup>1,2</sup>  and Jan Harms<sup>1,2</sup> <sup>1</sup>Gran Sasso Science Institute (GSSI), L'Aquila, Italy, <sup>2</sup>Laboratori Nazionali del Gran Sasso, INFN, Assergi, Italy

**Abstract** AUTHOR: Please check that authors' affiliations are correct. Gravity fluctuations produced by ambient seismic fields are predicted to limit the sensitivity of the next generation, gravitational wave detector Einstein Telescope at frequencies below 20 Hz. The detector will be hosted in an underground infrastructure to reduce seismic disturbances and associated gravity fluctuations. Additional mitigation might be required by monitoring the seismic field and using the data to estimate the associated gravity fluctuations and to subtract the estimate from the detector data, a technique called coherent noise cancelation. In this paper, we present a calculation of correlations between surface displacement of a seismic field and the associated gravitational fluctuations using the spectral element SPECFEM3D Cartesian software. The model takes into account the local topography at a candidate site of the Einstein Telescope at Sardinia. This paper is a first demonstration of SPECFEM3D's capabilities to provide estimates of gravitoelastic correlations, which are required for an optimized deployment of seismometers for gravity noise cancelation.

### 1. Introduction

A next generation of ground-based, gravitational wave (GW) observatories has been proposed including the European concept Einstein Telescope (ET) (ET Science Team, 2011) and the U.S. concepts Voyager (Adhikari et al., 2020) and Cosmic Explorer (Reitze et al., 2019). These detectors would have greatly improved sensitivity over almost the entire GW observation band compared to current generation detectors Virgo (Acernese et al., 2015), LIGO (Abbott et al., 2016), KAGRA (Akutsu et al., 2019), and LIGO India (Souradeep, 2016). Terrestrial gravity noise, also known as Newtonian noise (NN), constitutes one of the fundamental infrastructure limitations, which affects the sensitivity of GW detectors. NN originates from density fluctuations in the surrounding ground and atmosphere, causing a variation in the gravitational field, and these gravity fluctuations act on the test masses (TM) causing detector noise mostly below 30 Hz (Harms, 2019). A large sensitivity improvement is targeted with ET in the infrasound observation band (1 to 20 Hz), where current generations of detectors have no detection capabilities. This will increase the number and signal-to-noise ratio of observable GW signals and therefore significantly enhance the astrophysical impact of third-generation observatories (Hild et al., 2011; Maggiore et al., 2020). In the frequency band below 30 Hz, it is possible to follow better the inspiral phase of compact binaries composed of neutron stars (NS) and stellar-mass black holes (BH) or open the window to observations of intermediate-mass black holes (IMBH). It is possible to follow the waveform evolution for a longer amount of time, and this practically means: more accurate estimates of some of the binary systems parameters including its sky location (Grimm & Harms, 2020) and potentially an early warning for the electromagnetic (EM) follow-up of these sources (Chan et al., 2018). ET will also be sensitive to continuous GW emission from a large population of spinning NSs below 10 Hz (Sathyaprakash et al., 2012). Therefore, there is a strong scientific drive to expand the detection band and to improve the sensitivity down to lower frequencies.

The dominant noise sources at very low frequencies are those associated with the seismic motion that couples with the detector. One mechanism is the mechanical transmission, where ground vibrations perturb the motion of the TM via the TM suspension system. This is known as seismic noise. Elaborated vibration-isolation systems are used to suspend the TM, significantly reducing seismic disturbances within the detection band (Acernese et al., 2010; Matichard et al., 2014). Another mechanism is by gravitational coupling giving rise to NN and cannot be shielded in any way (Beker et al., 2011, 2015). A well-explored

cancellation scheme is based on Wiener filters (Badaracco & Harms, 2019; Cella, 2000; Coughlin et al., 2016, 2018). Wiener filters are linear filters calculated from the correlation between the reference and target channels (Orfanidis, 2007). In the context of seismic NN cancellation, the sensors (seismometers) monitor seismic fields, which means that correlations between them are to be expected (Harms, 2019).

Most of the seismic noise is generated near the surface, and it generally decreases significantly with depth. Predictions based on a detailed characterization of the LIGO sites show that seismic surface fields give the dominant contribution to NN (Driggers et al., 2012). Accordingly, a NN cancellation scheme can be realized using an array of seismometers deployed at the surface near the TM (Coughlin et al., 2016). The construction of ET has been proposed to be underground, where the amount of seismic motion is expected to be lower and more stable (Beker et al., 2015; Harms et al., 2010; Mandic et al., 2018). NN is about 2 orders of magnitude less underground which is substantial (Amann et al., 2020).

One of the most important things in NN cancellation is the homogeneity of the seismic field. Scattering of seismic fields from an irregular surface topography can cause heterogeneity of the seismic field. It can lead to a more complex field structure that is not completely characterized by surface displacement and will likely pose a great challenge even to 3-D seismic surveys with boreholes where effective placement of seismometers needs to be achieved (Badaracco & Harms, 2019). The scattering will especially be the problem if it is strong enough to alter seismic waveforms significantly over very short propagation distances (Driggers et al., 2012). Even if it is identified and fully characterized, scattering could pose a serious challenge to NN subtraction, since it might increase the required effort and therefore cost of a NN mitigation system. Issues of topographic scattering and its connection to NN cancellation are partly examined in M. Coughlin and Harms (2012). They found that the total contribution of waves scattered from topography can be high, which makes topographic scattering relevant to NN subtraction in future low-frequency GW detectors. Seismic scattering was investigated analytically in numerous publications; see, for example, Abubakar (1962, 1963), Gilbert and Knopoff (1960), Hudson (1967), and Ogilvy (1987). An extensive and conclusive study of the impact of topography scattering on coherent cancellation has not been carried out so far.

In this paper, we simulate synthetic ambient noise cross correlations between stations at the surface of a finite-element model using a 3-D spectral element method (SEM) implemented in SPECFEM3D Cartesian software (Komatitsch & Tromp, 2002a, 2002b; Komatitsch et al., 2018). Cross correlations are simulated for the flat model and for the topographic model using elevation data at the three (foreseen) vertices of the proposed ET site at Sardinia. Using these correlations, we show the effects of topographic scattering on seismic coherence and on correlations between TM acceleration and vertical seismic surface displacement. These correlations are crucial in Wiener filter construction. One of the main goals in the future will be to investigate whether high noise cancellation through Wiener filtering or similar methods will be effective at the Sardinia site for ET.

In section 2, the ET detector and the ET candidate site at Sardinia are briefly presented. In section 3, our main analysis tools SPECFEM3D Cartesian and Trelis are introduced. In section 4, the building of the finite-element model is described. In section 5, the theory of noise cross correlation is reviewed with focus on the method implemented in SPECFEM3D. In section 6, ensemble sensitivity kernels and their importance are explained. In section 7, we present the main results of our study concerning the effect of topographic scattering on seismic correlations and the prediction of gravitational coupling between seismic surface displacement and an underground TM.

## 2. ET and Sardinia Site

The third-generation GW observatory, ET, will be aiming to reach a sensitivity for GW signals emitted by astrophysical and cosmological sources about a factor of 10 better than current detectors over much of the observation band. The targeted observation band is from 3 Hz to a few kilohertz with a strain sensitivity of about  $10^{-24} \text{ Hz}^{-\frac{1}{2}}$  within this band (ET Science Team, 2011; Hild et al., 2011). As all of the GW detectors so far, ET will be a modified Michelson interferometer with suspended mirrors that act as TMs. These instruments behave as transducers to convert the space-time strain caused by a GW to fluctuations in optical power (Barsotti et al., 2019). In its final construction stage, ET should consist of three nested detectors, built a few 100 m underground, which would be arranged in a triangular pattern. Advantages of ET with respect to the traditional L-shaped geometry of current GW detectors are that it will have a more uniform antenna pattern and be sensitive to both GW polarizations independent of the wave propagation direction. Each individual

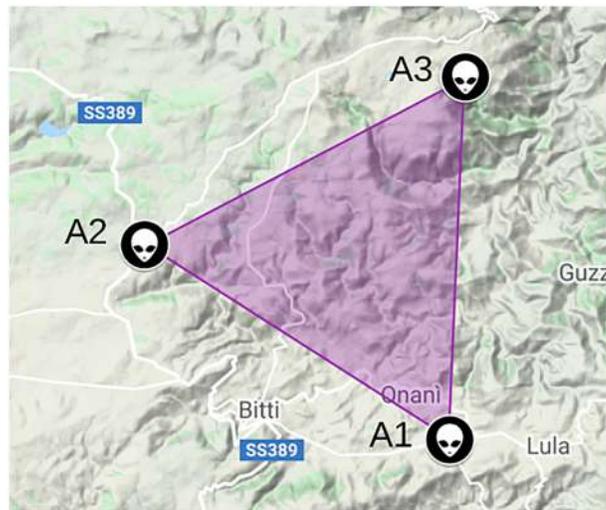


**Figure 1.** Sardinia candidate site for Einstein Telescope with marked vertex locations.

detector will comprise two interferometers forming a so-called xylophone configuration (Hild et al., 2009), one specialized for detecting low-frequency GWs (low laser power, low temperature, frequency range from 3 to 50 Hz) and the other one for the high-frequency part (room temperature, high laser power, frequency range from 50 to 10 kHz).

For the reduction of NN, a detector site with weak gravity fluctuations should be chosen. High-frequency seismic spectra (above a few kilohertz) are all significantly quieter underground than at typical surface sites (Beker et al., 2015; Harms et al., 2010; Mandic et al., 2018). This can be explained by the exponential fall of Rayleigh wave amplitudes combined with the fact that high-frequency seismicity is typically generated at the surface, and most surface sites are covered by a low-velocity layer of unconsolidated ground. Also, underground sites are attractive since the risk that anthropic seismic noise will change in the future due to surface infrastructural developments like the construction of industry or traffic roads is lower (Beker et al., 2015). Additionally, atmospheric gravity perturbations are strongly suppressed underground (Fiorucci et al., 2018).

The selected site should offer the possibility for efficient coherent cancelation of NN with surface and bore-hole seismometer deployment. Two-point spatial correlation of the seismic field determines the efficiency of a cancelation scheme. The strongest scatterer of seismic waves above a few Hertz is the surface with rough topography (strong topographic gradients). If scattering is significant, then correlation can be strongly altered, and a seismic array consisting of a potentially large number of seismometers needs to be deployed with difficulty to determine sensor positions (Harms, 2019). Since the ground medium close to the TM at the Sardinia site is fairly uniform, high scattering cross sections are unlikely to be observed for underground propagation of seismic waves (Driggers et al., 2012). Still, heterogeneity of the ground may add complexity, and a refined model should include information about local geology.

The suggested site at Sardinia (Italy) is near the city Lula (Figure 1) with vertex coordinates given in Table 1.

Spectral density of the Sardinia site ambient seismic field is close to Peterson's New Low Noise Model (NLNM), and there is no strong daily or seasonal variation above a few Hertz (Beker et al., 2012, 2015). Also, what goes in favor of the Sardinia site is the fact that the most seismically quiet sites are found in

**Table 1**  
*Coordinates of Vertices of Einstein Telescope*

Cavern	Latitude	Longitude
A	40°28'21.11"	9°27'18.78"
B	40°31'27.73"	9°20'54.84"
C	40°34'08.24"	9°27'38.82"

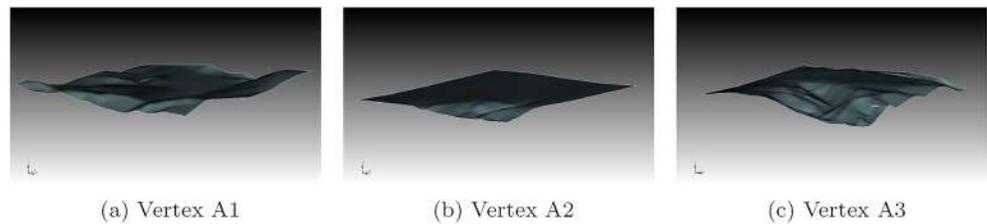


**Figure 2.** (a–c) Elevation data at the three vertex locations of Einstein Telescope over areas with 3 km side lengths.

hard rock geologies and the Sardinia site is mostly made of granite and schist. In terms of the construction of underground facilities, rock stability is a crucial factor, which then tends to be more favorable in hard rock (Beker et al., 2015). This is disadvantageous for NN reduction with depth, which decreases exponentially with increasing seismic wave speed. Coordinates of vertices were chosen taking into consideration the quality of the rocks.

These vertices make an equilateral triangle with approximately 10.7 km side length. Surface areas of 3 km  $\times$  3 km size with topographies where the respective ET vertex is located under the center point of the area are given in Figure 2. The resolution of elevation data is 30 m. For examination of seismic coherence and gravity displacement correlations, due to high computational costs (and, for this study at least, due to limited computational resources of only about 100 nodes), we chose only vertex A3 because it has the roughest surrounding topography (Figure 2c) among all three vertices and therefore the largest scattering potential. Roughness can, for example, be quantified by the rms of the elevation data, which are 52.4, 43.5, and 129.6 m for the Vertices A1, A2, and A3, respectively. As already said, scattering causes heterogeneity of the seismic field, which will be one of the main problems in NN cancellation. If the problem of NN description and cancellation is understood for Vertex A3, there will not be any additional challenges when repeating the analysis for Vertices A1 and A2.

### 3. Finite-Element Simulation and Model Meshing

SPECFEM3D Cartesian is a powerful software package for seismic wave propagation modeling at local and regional scales based upon the SEM (Komatitsch et al., 1999; Komatitsch & Tromp, 1999). The SEM is a highly accurate numerical method, which combines the geometrical flexibility of the finite-element method with the fast convergence associated with spectral techniques, and it has origins in computational fluid dynamics (Maday & Patera, 1989; Patera, 1984; Seriani & Priolo, 2012). It uses a mesh of hexahedral finite elements on which the wave field is represented in terms of high-degree Lagrange polynomials on Gauss-Lobatto-Legendre interpolation points. SEM is more accurate than widely used classical techniques such as the finite-difference method (Olsen et al., 1997; Virieux, 1986), in particular for surface waves (Komatitsch & Tromp, 1999, 2002a), which play an important role in ground motion seismology (Komatitsch, 2004). It is also very well suited to parallel implementation on supercomputers and clusters of CPUs or GPUs (Komatitsch et al., 2003, 2008; Tsuboi et al., 2003). SPECFEM3D software is written in Fortran2003 with full portability in mind (Komatitsch et al., 2018). The package uses the parallel algorithm based upon the Message Passing Interface (MPI) (Gropp et al., 1994; Pacheco, 1997).

We used Trelis for the creation of models and their exporting into a SPECFEM3D Cartesian file format. Trelis is a full featured software for generation of two-dimensional and three-dimensional finite-element grids (meshes) and geometry preparation (Blacker et al., 2019). Generating meshes for complex model-based geometries requires a variety of tools, and many of them in Trelis are completely automatic. In creating a load-balanced, partitioned mesh, it is needed to set up a hexahedral mesh, in which goes a large amount of work, then to export that mesh into a SPECFEM3D Cartesian file format and to partition it for a chosen number of cores in SPECFEM3D. The next step is creating the distributed databases in which all the missing information needed by the SEM solver are created. The final step is to run the solver (Komatitsch et al., 2018). Creating the databases and running the solver in SPECFEM3D is done on parallel on a number of cores chosen while partitioning.

Besides earthquake simulations, SPECFEM3D Cartesian includes functionality for seismic noise tomography as well. It can perform noise cross-correlation simulations. At the end of noise cross-correlation

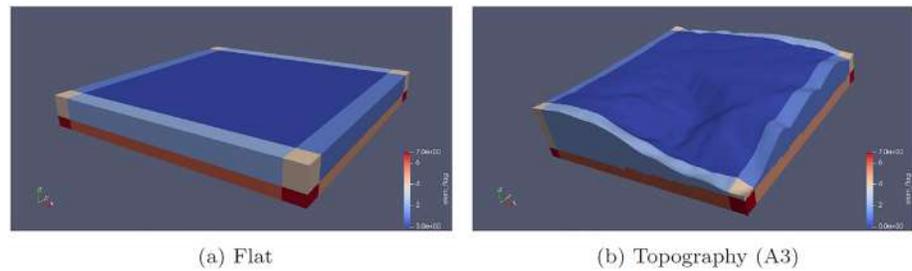


**Figure 3.** (a, b) Models with convolutional perfectly matched boundary layers (C-PML).

simulations, two outputs are the most interesting: the simulated ensemble cross correlations and the so-called ensemble sensitivity kernels, which quantify how much a correlation depends on properties of the ground medium throughout the model. Cross correlations are generated based on a SEM (Komatitsch & Tromp, 1999; Komatitsch & Vilotte, 1998), and ensemble finite-frequency sensitivity kernels are generated based on an adjoint method (Liu & Tromp, 2008; Tromp et al., 2005).

#### 4. Model Setup

Before running simulations using created models, a time-consuming step is to set up appropriate absorbing boundary conditions. In order to simulate a semi-infinite medium, absorbing conditions are used on all sides of the model except the free surface. If absorbing boundary conditions are not good enough, there are significant artificial boundary reflections from the numerical model which affect cross correlations. The convolutional perfectly matched layers (C-PML) absorbing boundary condition are very efficient from a numerical point of view for the elastic wave equation in absorbing body waves with nongrazing incidence and surface waves (Komatitsch & Martin, 2007). C-PML has better absorbing efficiency, especially in the case of small mesh size than commonly used Clayton-Enquist absorbing boundary conditions which are mostly sufficient in the case of large mesh size (Komatitsch, 2004).

In order to create quality absorbing boundary layers out of the edge elements/layers of the meshed model, it is important to have those elements/layers as regular as possible with constant thickness and aligned with the coordinate grid axes ( $X$ ,  $Y$ , and/or  $Z$ ). The thickness of C-PMLs can be different for the  $X$ ,  $Y$ , and  $Z$  sides but must have a fixed, specific value for each coordinate individually. Usually, three or four C-PMLs on each of five absorbing model surfaces are sufficient, but as simulations showed, having more C-PMLs on each of the absorbing surfaces suppressed reflections more, regardless of the thickness of the single C-PML. A C-PML is very efficient, but it does not absorb incident waves completely (see Figure 7). In order to prevent remaining parasitic waves to affect cross correlations, that is, to reach receivers, simulation time is set to be quite low (0.94 s). The thickness of the overall C-PML used for the flat surface model is 210, 210, and 120 m for the  $X$ ,  $Y$ , and  $Z$  boundary planes, respectively (Figure 3a) and for the topography model 179, 174, and 179 m (Figure 3b). More information about C-PML can be found in Komatitsch and Martin (2007), Martin and Komatitsch (2009), Martin et al. (2010), and Xie et al. (2014).

The important parameter values of the model are  $v_p = 3,500$  m/s compressional wave speed,  $v_s = 2,000$  m/s shear wave speed, and  $\rho = 2,750$  kg/m<sup>3</sup> for the uniform mass density based on the fact that at the suggested site, granite and partly schist prevail and also based on recent geoseismic studies (Giunchi et al., 2020). The simulations were performed without attenuation and anisotropy. We do not have any robust information about attenuation and anisotropy in this area yet. In addition, attenuation is not yet supported for noise cross-correlation simulations with SPECFEM3D. However, it can also be expected that attenuation plays a negligible role over the small extent of the medium relevant to gravity noise calculations.

C-PML absorbing boundary condition is only supported in CPU mode for now (so one cannot use GPUs). Using GPUs would, of course, make the running of simulations much faster. Also, C-PML is still under test for the third step of cross-correlation simulations-adjoint simulations.

The horizontal size of the models is  $3 \text{ km} \times 3 \text{ km}$  with a depth of 360 m in the flat free surface case (Figure 4a) and with variable depth in the case with A3 topography. The minimum depth is 192 m, and the maximum is 798 m (Figure 4b). Mesh size of the flat free surface model is 30 m (for all three dimensions). For the topography model, it varies from 12 to 71 m in  $Z$  dimension. For  $X$  and  $Y$  dimensions, it is 25 m. Mesh

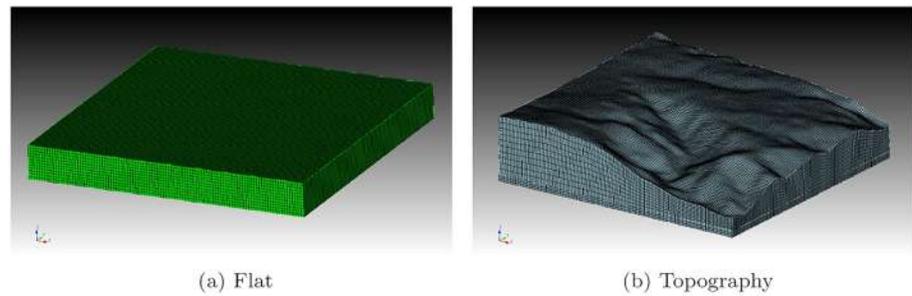


**Figure 4.** (a, b) Meshed models.

properties play an important role in estimating the stability of the simulation and estimating the maximum frequency, up to which synthetics are valid. Stability of simulations depends on  $P$  wave velocity, time step size, and minimum distance between Gauss-Lobatto-Legendre interpolation points. From these parameters, one can calculate the Courant number that is used as measure of stability of the simulation. We also made sure that the maximum frequency lies above the target band, that is, above 30 Hz. Other important aspects of mesh design are governed by the meshing software Trellis.

As already said, the results of simulations are valid up to a certain maximum frequency (minimum period). This maximum frequency depends on the mesh size and  $S$  wave velocity, and for the flat, free surface model, it is 53 Hz (and it is constant throughout the model) and for the topography model it varies between 22 and 66 Hz. Minimum periods up to which simulations at the A3 vertex are valid in specific mesh elements are shown for the topography model in Figure 5. The minimum period is an estimation, and there is no sharp cutoff period for valid synthetics. Correlations become just more and more inaccurate for periods shorter than this estimate. From what we saw from simulations, they are usually sufficiently accurate only up to about 10 Hz from estimated values, and this value does not only depend on the mesh size and density but also on details of the seismic source modeling.

Source distribution affects surface waves amplitudes (Tsai & Moschetti, 2010), it influences correlograms, and its knowledge is important to correctly interpret the data (Basini et al., 2012; Hanasoge et al., 2012). For cross-correlation simulations, the distribution of noise sources in SPECFEM3D Cartesian is constrained to the surface, which is not a major drawback since the most relevant seismic sources in the NN band are expected to be surface sources. Also, we defined the ensemble of seismic sources used for the cross-correlation simulation to have a minimum distance to the center of the model surface since we assume that these areas will be protected in the future, that is, excluding the presence of strong seismic sources inside the protected area. The radius of this area was also varied in our study to see the impact on seismic spectra and correlations. This also implies that the ET infrastructure must not introduce significant perturbations itself, which requires a novel low-noise infrastructure design avoiding some of the errors made with current detector infrastructure.

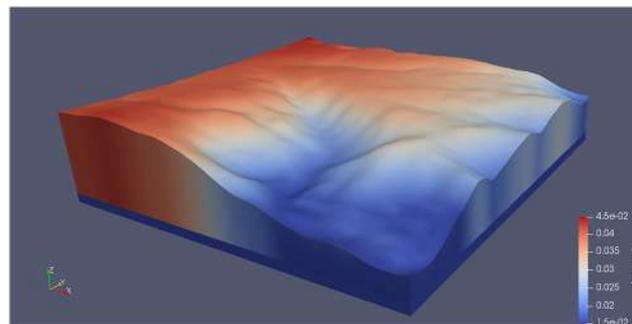


**Figure 5.** Minimum wave period resolved in each element of A3 topography model.

## 5. Noise Cross-Correlation Simulations

Ambient noise seismology is of great relevance to high-resolution crustal imaging. Thanks to the unprecedented dense data coverage, it affords in regions of little seismicity (Basini et al., 2012). Cross correlations between seismograms that recorded diffuse seismic wavefields created by stochastic wave excitation at the Earth's surface at different seismographic stations show statistically significant signals to be present (Tromp et al., 2010). A common interpretation of noise cross correlations is to relate them to a form of the Greens function between two receivers (Fan & Snieder, 2009; Lobkis & Weaver, 2001; Montagner et al., 2012; Wapenaar et al., 2006). The method implemented in SPECFEM3D is best described in Tromp et al. (2010), where it extends to the application of tomography and evaluating misfits between models and observations.

The solution for boundary problems of the elastodynamic equation can be expressed with the help of Green's tensor  $\mathbf{G}$

$$\mathbf{s}(\mathbf{x}, t) = \int_{-\infty}^t \int_{\Omega} \mathbf{G}(\mathbf{x}, \mathbf{x}'; t - t') \cdot \mathbf{f}(\mathbf{x}', t') d^3\mathbf{x}' dt'. \quad (1)$$

The Greens tensor satisfies the relationship (Aki & Richards, 2009; Dahlen & Tromp, 1998)

$$\mathbf{G}(\mathbf{x}, \mathbf{x}'; t - t') = \mathbf{G}^T(\mathbf{x}', \mathbf{x}; t - t'). \quad (2)$$

In frequency domain, the solution can be expressed using the Fourier transform

$$\mathbf{s}(\mathbf{x}, \omega) = \int_{\Omega} \mathbf{G}(\mathbf{x}, \mathbf{x}'; \omega) \cdot \mathbf{f}(\mathbf{x}', \omega) d^3\mathbf{x}'. \quad (3)$$

In practice, one uses an ensemble average of many cross correlations, which we will refer to as the *ensemble cross correlation*. One of the most important data processing techniques in all of the ambient noise seismology is ensemble averaging, allowing to reduce the effects of a set of scatterers and sources randomly distributed in time and space to those of a diffuse wavefield (Basini et al., 2013). Ensemble-averaged cross correlations between synthetic seismograms at two geographically distinct locations on the free surface are determined under the assumption that noise is spatially uncorrelated but nonuniform. We focus our study on seismic surface measurements, despite the advantages of deeper seismometer installations (Mandic et al., 2018).

Let us consider the  $\hat{\mathbf{v}}^\alpha$  component of the displacement at location  $\mathbf{x}^\alpha$  and the  $\hat{\mathbf{v}}^\beta$  component of the displacement at location  $\mathbf{x}^\beta$ :

$$s^\alpha(t) \equiv \hat{\mathbf{v}}^\alpha \cdot \mathbf{s}(\mathbf{x}^\alpha, t), \quad s^\beta(t) \equiv \hat{\mathbf{v}}^\beta \cdot \mathbf{s}(\mathbf{x}^\beta, t). \quad (4)$$

The cross correlation between those two time series is given by

$$C^{\alpha\beta}(t) = \int s^\alpha(t + \tau) s^\beta(\tau) d\tau. \quad (5)$$

We assume that sources of the field are spatially uncorrelated, which implies

$$\langle f_j(\mathbf{x}', t') f_m(\mathbf{x}'', t'') \rangle = S_{jm}(\mathbf{x}', t' - t'') \delta(\mathbf{x}' - \mathbf{x}''), \quad (6)$$

where  $\langle \cdot \rangle$  denotes an ensemble average (Woodard, 1997).  $S_{jm}$  describes the geographic and geometric properties and  $\omega$  dependence of the noise sources; it is nonzero only at the (surface) locations of the seismic sources.

Using Fourier transform, a representation in terms of Green's tensor and taking into consideration ensemble average and Equation 2, the analytical expression for ensemble cross correlation is

$$\langle C^{\alpha\beta} \rangle(t) = \frac{1}{2\pi} \hat{v}_i^\alpha \hat{v}_\ell^\beta \iint S_{jm}(\mathbf{x}, \omega) G_{ji}(\mathbf{x}, \mathbf{x}^\alpha; \omega) G_{m\ell}^*(\mathbf{x}, \mathbf{x}^\beta; \omega) \exp(i\omega t) d^3\mathbf{x} d\omega. \quad (7)$$

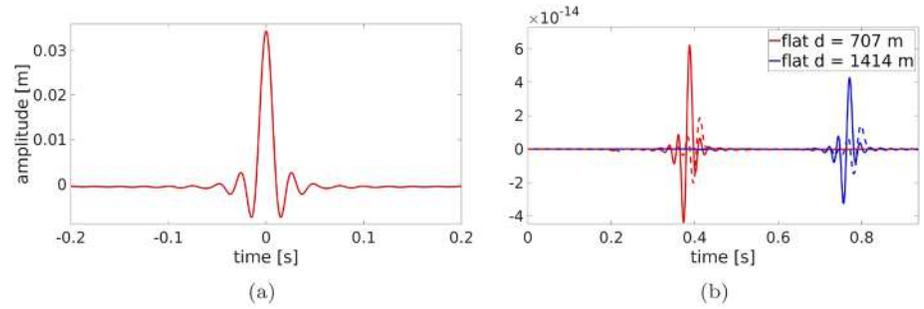


**Figure 6.** Source time function corresponding to the noise spectrum (a) and vertical displacement of generating wavefield for the flat and topography models at the locations with 707 and 1,414 m distance from the source (b). The dashed, colored curves in (b) mark with corresponding colors the vertical displacement of generating wavefield with topography.

One may notice that ensemble cross correlations have the symmetry:

$$\langle C^{\alpha\beta} \rangle (t) = \langle C^{\beta\alpha} \rangle (-t). \quad (8)$$

The more detailed calculation can be found in Tromp et al. (2010).

Our noise cross-correlation simulations require two steps. In the first step, one calculates a generating wavefield obtained by inserting a source time function at the location of the first receiver. The source time function of the generating wavefield is obtained using the spectrum of the ensemble-averaged noise, and it is narrowly concentrated around zero time. We use a source time function shown in Figure 6a representing a frequency-independent seismic spectrum in the interesting frequency range (1–30 Hz), since the absolute values of the seismic spectrum are not relevant for this paper. Generally, results in frequency domain can be rescaled using realistic/observed seismic spectra when needed.

Then, the results of the generating wavefield are saved at each time step at locations where the actual noise sources are located, which in our simulation covers an area of the free surface. Displacement in the vertical direction of the generating wavefield for the flat and topography models at two locations with different distances from the source is shown in Figure 6b.

Next, in the second step, one uses this generating wavefield at the locations of the noise sources as sources of the ensemble forward wavefield associated with the first receiver. We assume that the excitation is along the vertical direction of the surface. In the case of vertical forces, more than two thirds of the total energy is radiated as Rayleigh waves (Woods, 1968). Regarding our application, at the surface, the relative amount of Rayleigh waves is even larger (Sanchez-Sesma & Campillo, 1991). It should also be noted that in our models, which basically represent a homogeneous half-space, no other modes of Rayleigh waves, apart from the fundamental Rayleigh mode, are possible. The source of the ensemble forward wavefield is just the time-reversed generating wavefield. The ensemble cross correlation is equal to the  $\mathbf{v}^\alpha$  component of the ensemble forward wavefield  $\Phi^\beta$  evaluated at location  $\mathbf{x}^\alpha$ :

$$\langle C^{\alpha\beta} \rangle (t) = \mathbf{v}^\alpha \cdot \Phi^\beta (\mathbf{x}^\alpha, t). \quad (9)$$

Having in mind Equation 8, it is clear that knowing either  $\Phi^\alpha$  or  $\Phi^\beta$ , the ensemble cross correlation can be calculated. More details can be found in Tromp et al. (2010). A sequence of snapshots resulting from a simulation of the wavefield with a source at the center of the model surface with the source time function as in Figure 6a can be seen in Figure 7 for the flat model and in Figure 8 for the A3 topography model.

## 6. Sensitivity Kernels

Another step can be taken with noise cross-correlation simulations to obtain sensitivity kernels, which quantify the sensitivity of the cross correlations to parameters of the ground medium such as mass density and seismic speeds. In addition to the generating and ensemble forward wavefield described in section 5, the calculation of sensitivity kernels requires another wavefield called ensemble adjoint wavefield. The sensitivity kernel results from an interaction between the ensemble forward wavefield and the ensemble adjoint

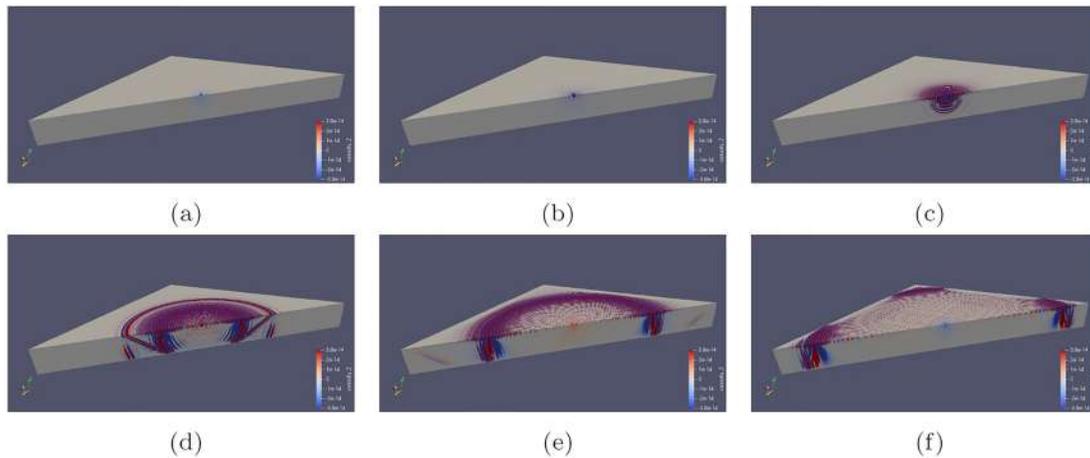


**Figure 7.** (a–f) Propagation of seismic waves for the flat surface model using a source time function determined by the spectrum of the ensemble-averaged noise.

wavefield. It is then possible to estimate sensitivity kernels without requiring computationally expensive ensemble averages as done in practice when analyzing seismic data (substituting ensemble averages by temporal averages). As a technical note, the calculation of sensitivity kernels with SPECFEM3D does not currently support C-PML. We used Clayton-Enquist boundary conditions for these simulations.

In seismology, sensitivity kernels are very important for tomographic inversion and can be used to improve Earth and source models. They illuminate those parts of models that are inaccurate. In other words, using observed correlations and making simulations of synthetic correlations, one uses the cross-correlation misfit to iteratively improve the model. More about ensemble adjoint wavefield and sensitivity kernels can be found in Liu and Tromp (2006), Tromp et al. (2005, 2008, 2010), and Peter et al. (2011). Sensitivity kernels are not of direct relevance to our work, but they give additional information whether the model size is sufficiently large for the simulation of correlations, in which case sensitivity kernels should be small toward the boundaries of the model. For the future, they can guide the development of more sophisticated models with inhomogeneous geology.

The theoretical work in Tromp et al. (2010) shows how adjoint techniques (e.g., Peter et al., 2007; Tromp et al., 2005) can be applied to ambient noise seismology taking into account the nonuniform distribution of noise sources. The ensemble adjoint wavefield is produced by a source located at the second receiver whose time function depends on the misfit between simulated and observed correlations. There are various possibilities to evaluate cross-correlation misfits. The method chosen in SPECFEM3D is based on the misfit

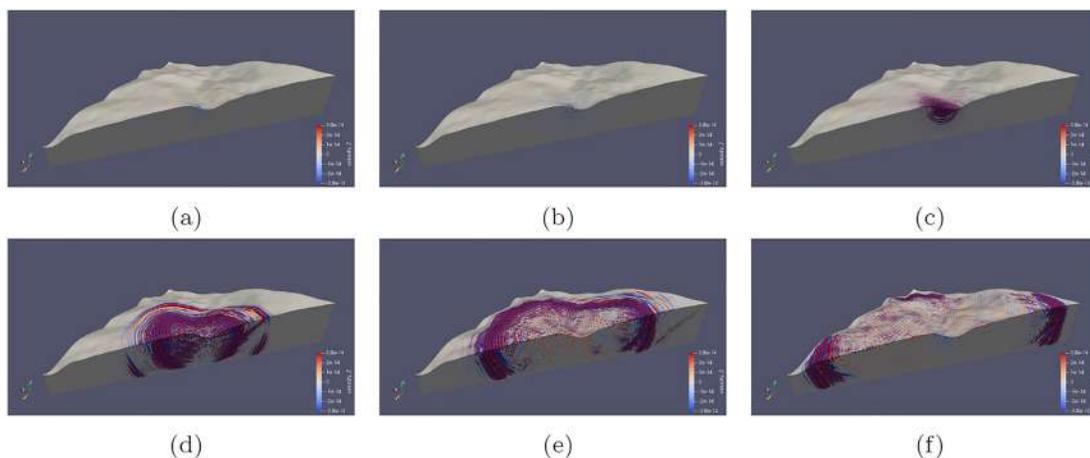


**Figure 8.** (a–f) Propagation of seismic waves for the A3 topography model using a source time function determined by the spectrum of the ensemble-averaged noise.

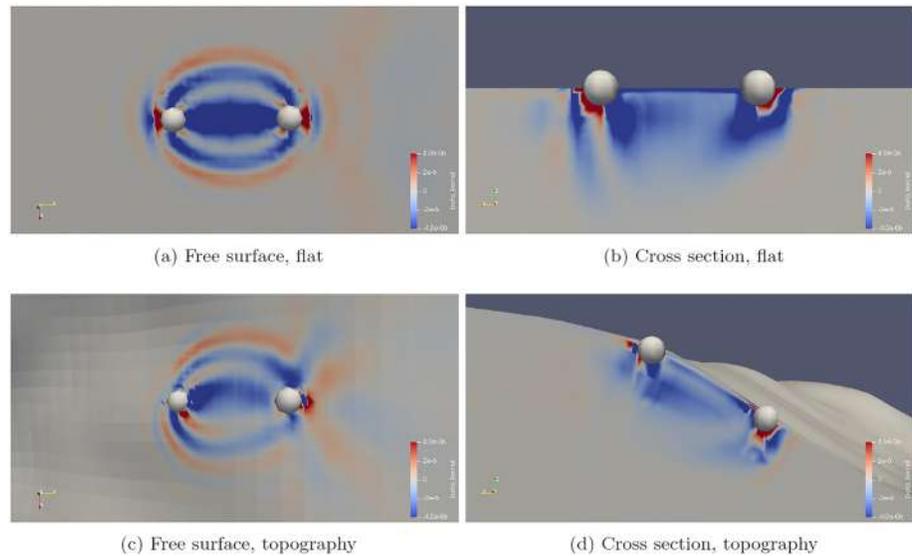


**Figure 9.** Beta kernel for flat (a, b) and topography surface model (c, d). White spheres represent receivers at a distance of 130 m from each other.

of cross-correlation delay times. The cross-correlation delay time would, for example, be responsible for a complex phase of cross-spectral densities between sensors. Since we are only interested in the sensitivity kernel and not in the actual inference of ground properties using seismic observations, an arbitrary misfit of  $\Delta T = 1$  s is chosen (Tromp et al., 2010).

The ensemble adjoint source corresponding to a delay time misfit involves the first time derivative of the simulated ensemble cross correlation  $\langle \dot{C}^{\alpha\beta} \rangle$ . As will be shown subsequently, ensemble cross correlations are dominated by Rayleigh surface waves, whose main sensitivity is to shear wave speed (often given the symbol  $\beta$ ). So here, we focus on beta kernels. The beta kernel is a volumetric field representing the gradient of the misfit function with respect to  $S$  wave speed.

The beta kernel is shown in Figure 9 for the flat (a, b) and for the A3 topography model (c, d). One can see that cross correlations are most sensitive to properties of the ground close to and between the two receivers and close to the surface. Note that the kernel is asymmetric with respect to an exchange of receivers. This asymmetry comes from the fact that kernels are defined for two branches, the so-called positive and negative branch (the positive branch being shown). The positive branch describes cross correlations whose time delays are consistent with waves reaching the second receiver before the first.

If we interpreted the 1 s time delay as an observed misfit, then the plots in Figure 9 would tell us that the  $S$  wave speed in the region between the two receivers, since the kernel is negative here, would have to be decreased to reduce the time delay misfit between observation and model. The sign of the kernel would be inverted in the negative branch since the model would have to be corrected to increase a negative time delay.

## 7. Results

ET targets GW observations down to a few Hertz (Punturo et al., 2010), which means that seismic NN will play an important role for instrument design. The detector will be hosted in an underground infrastructure, which creates a low-noise environment providing an essential reduction of NN. Detector infrastructure including pumps and ventilation must not disturb the underground environment or be at a safe distance to the TM. Further mitigation of NN can be achieved by noise cancellation using an extensive monitoring system of the ambient seismic field (Harms, 2019). The idea is to pass seismic data through a filter such that its output can be understood as a coherent estimate of seismic NN and be subtracted from the GW data (Cella, 2000). These filters can take the form of Wiener filters calculated from the correlations between seismometers and the GW detector. The most challenging aspect of this technology is to determine the locations of a given number of sensors that optimize the cancellation performance (Badaracco & Harms, 2019; Coughlin et al., 2016).

Rayleigh waves are predicted to give the dominant contribution to NN in surface detectors (Coughlin et al., 2016; Harms et al., 2020), and even underground detectors can still be limited by gravitational noise from Rayleigh waves depending on the detector depth (Badaracco & Harms, 2019). The Rayleigh field produces surface displacement and density perturbations beneath the surface at the same time (Beccaria et al., 1998; Hughes & Thorne, 1998), which leads to gravity perturbations. Even if we do not know the wave composition of a seismic field at a site, it is still reasonable in many cases to assume that Rayleigh waves dominate the normal surface displacement at frequencies in the range 1–20 Hz produced by surface or near-surface seismic sources (Bonney-Claudet et al., 2006; Mooney, 1976). Only at exceptionally quiet (necessarily remote) surface sites or underground sites, body wave content is expected to be significant or dominant in this band (however, mode content can change significantly with time if due to natural sources; Coughlin et al., 2019).

In the following, we present results of our analyses of spatial correlations in an ambient seismic field simulated with SPEC3D, and we predict the correlation between surface seismometers and the gravity perturbation experienced by an underground TM, which is the crucial information for the optimization of surface arrays for NN cancellation. As already explained, our analyses are constrained by the computational resources that were available to us. One consequence is that it was not possible to run a simulation with a TM depth greater than 100 m (while 200–300 m is the envisioned depth of ET TM), since this would have required a dense set of receivers distributed over a much larger surface area. We learn from these results how topography impacts correlations, which we expect to be the main site effect on seismic correlations and seismic gravitational noise.

### 7.1. Seismic Scattering

The effect of scattering of seismic waves from surface topography on seismic correlation and gravity perturbations of TM needs to be quantified using the methods outlined in section 5. As mentioned earlier, because of the way we choose to excite seismic waves in this analysis, the ensemble forward field is mainly composed of Rayleigh surface waves. For flat, free surfaces, Rayleigh waves, once decoupled from the near field of the seismic sources, propagate without conversion into other seismic modes.

The scattering by topography depends on the size of elevation changes, area of contact, and the length scale of the irregularity. It also depends significantly on incident angle and type of seismic waves propagating through the area. Amplitudes of scattered waves should increase linearly with the size of elevation changes for small obstacles according to perturbation theory based on the first-order Born approximation (Gilbert & Knopoff, 1960). Born approximation breaks down for steeper slopes (steeper than approximately 30°) and higher elevations of topography (depending on wavelength of seismic waves and horizontal dimension of topography), for which there is strong amplification of scattered waves (Hudson et al., 1973; Snieder, 1986). Therefore, the scattering should be much reduced in the case of irregularities with gentle curvature when compared with irregularities (mountains) with abrupt discontinuities in curvature (bluff topography) (Gilbert & Knopoff, 1960). An important point is that the incident wave is essentially “blind” to features that are much smaller than a wavelength (Otto, 1977). Scattering always becomes weaker at smaller frequencies if all other parameters are kept constant, but generally, there is no simple frequency scaling valid for the entire wavenumber space. Scattering coefficients in wavenumber space are mainly proportional to the topographic spectrum (M. Coughlin & Harms, 2012). The maximum scattering is generally present when seismic wavenumbers match the wavenumbers of the topographic spectrum (Hudson & Knopoff, 1967).

In our ensemble forward wavefield, there is also body wave content. So it is interesting to see what happens with body waves during scattering in addition to the dominant Rayleigh wave field. In the case of incident *S* waves, if the dominant horizontal length scales of the surface spectrum are small compared with the length of incident waves, the amplitudes of some of the scattered waves decrease exponentially with depth similar to Rayleigh waves. A periodic surface characterized by short horizontal length scales traps more of the incident energy than one characterized by longer length scales, but the amount of trapped energy also depends on the associated amplitudes of the topographic spectrum. This trapped energy feeds into the surface waves (Abubakar, 1962).

For the incident *P* waves, scattered waves are mostly Rayleigh waves accompanied by a weaker (horizontal) *P* wave (Bard, 1982). The amplitude ratio of scattered Rayleigh to incident longitudinal wave depends mostly on angle of incidence and horizontal and vertical dimensions of the corrugation. For example, for normally incident longitudinal waves, with Rayleigh wavelength equal to the width of corrugation, amplitude ratio

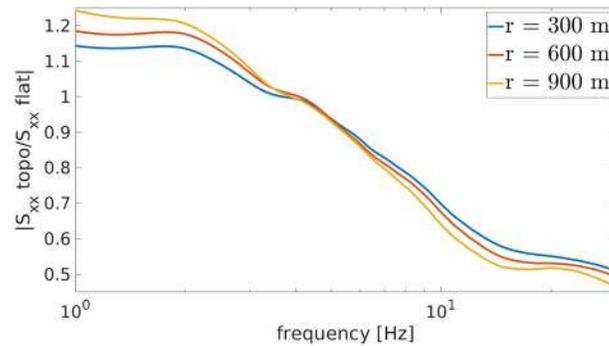


**Figure 10.** Ratio of seismic spectral densities at the center of topographic (A3 vertex) and flat models for different values of the minimal distance of seismic sources.

grows linearly with ratio of horizontal and vertical dimensions of the corrugation. Already at ratios of horizontal and vertical dimensions less than one, scattered Rayleigh wave has surface amplitude that is greater than that of the incident longitudinal wave alone (Hudson et al., 1973). In conclusion, a significant percentage of bulk waves scatter into Rayleigh waves and additionally that scattering is driven by high-wavenumber components of the surface topography, which typically have weaker amplitudes.

For incident Rayleigh waves, which is the most interesting case for us, scattering effects were investigated in Maradudin and Mills (1976). The main conclusion that one may draw from there is that the predominant contribution from the roughness-induced scattering of the incident Rayleigh wave is into other Rayleigh waves. At low frequencies, the ratio between scattered Rayleigh and bulk waves is about 10, and it grows as the frequency increases. So Rayleigh wave/Rayleigh wave scattering contribution is about an order of magnitude larger than the bulk wave contributions. However, details depend on the topography.

Scattering especially from Rayleigh waves into Rayleigh waves is a very efficient scattering channel, but since it does not cause a change in wave type, its impact on NN cancellation can easily be modeled. Still, it is found that topographic scattering might be relevant to NN subtraction in regions with rough topography (M. Coughlin & Harms, 2012). Fields of scattered waves do not generally permit a unique correspondence between frequency and wavelength, since at each frequency, the wavenumber spectrum of the scattered field is typically continuous. This is the main challenge for the design of a NN cancellation system in seismic fields with significant contributions from scattered waves. We need to mention that also scattering from underground caverns of the ET would significantly modify the seismic field in the vicinity of the cavern, but the impact on NN remains small as long as the caverns are much smaller than the seismic wavelengths in the relevant frequency range (Harms, 2019).

As a first characterization of topographic scattering, we calculate the ratio of power spectral densities at the center of our models with and without topography. The ratio is shown in Figure 10 between 1 and 30 Hz for three different minimal distances of seismic sources to the center point. The plot shows that higher frequencies are more scattered out with respect to lower frequencies by topography. In other words, topography acts as a low-pass for Rayleigh waves protecting a point to some extent from the influence of distant seismic sources. At the A3 vertex of the ET, topographic protection is provided down to about 4 Hz. As can be seen, the ratio depends weakly on the minimal distance of seismic sources, which can be explained by the contribution of increasingly large topographic scales to the scattering coefficients. Of course, the absolute value of power spectral density reduces significantly when sources are more distant.

## 7.2. Seismic Coherence

The SPECSEM3D simulation of seismic correlations yields a time domain correlation  $C_{ij}(\tau)$  between two receivers. For our analysis, we need the Fourier transform,

$$S_{ij}(f) = \int_{-\infty}^{\infty} d\tau C_{ij}(\tau) e^{i2\pi f\tau}, \quad (10)$$

which, according to the Wiener-Khinchin theorem, is the cross power spectral density (CPSD) between the two sensors. The CPSD can be normalized so that its absolute value lies between 0 and 1, a quantity called *coherence*:

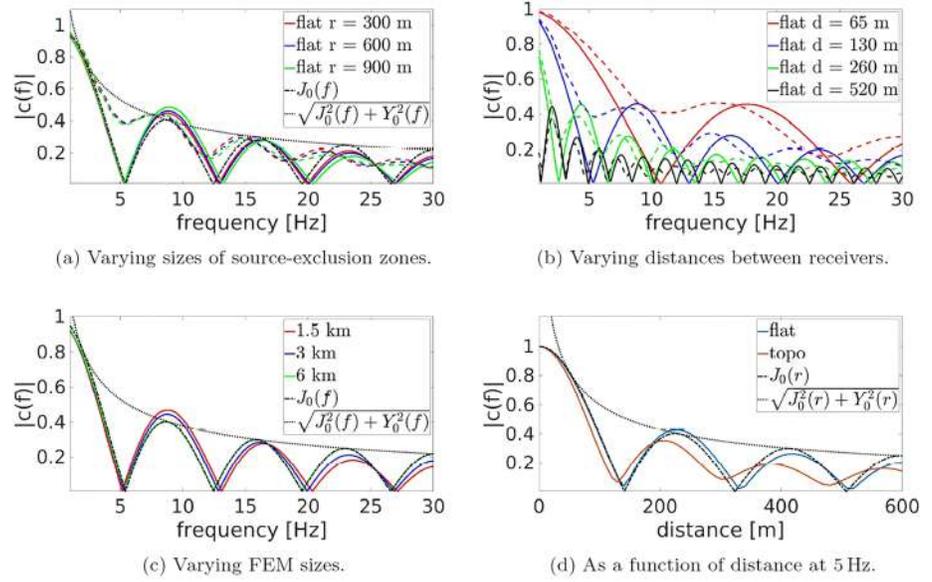


**Figure 11.** (a–d) Plots of seismic coherence calculated by SPEC3D. The dashed, colored curves in (a) and (b) mark with corresponding colors the coherence with topography.

$$c_{ij}(f) = \frac{S_{ij}(f)}{\sqrt{S_i(f)S_j(f)}}. \quad (11)$$

Figure 11 summarizes four analyses of seismic coherence with SPEC3D. In plot (a), we show the absolute value of coherence for the flat surface and A3 topography models with varying minimal distances of seismic sources of the ambient field. While the coherence is significantly different between the two models, it only depends weakly on the minimal distance of sources. The plot also contains an analytical prediction of coherence for the flat surface, isotropic Rayleigh wave field, where the coherence is given by a Bessel function

$$c_{ij}(f) = J_0(2\pi f |\vec{r}_j - \vec{r}_i|/c) \quad (12)$$

with a Rayleigh wave speed of  $c = 1,840$  m/s. In this simple case, the coherence is real valued, but it is generally a complex quantity. The distance between the two receivers is 130 m.

Plot (b) displays the absolute value of coherence for varying distance between the two receivers. Again, the coherence obtained from the A3 topographic model is qualitatively different from the flat surface coherence for all distances between receivers. With the A3 topographic model,  $|c_{ij}(f)|$ , does not vanish at any frequency, which is likely due to a mixed wave content with Rayleigh waves and scattered waves of different wavelengths.

In plot (c), we verify that the size of the standard finite-element model ( $3 \text{ km} \times 3 \text{ km}$ ) was not chosen too small for analyses in this paper, that is, that coherence changes weakly when increasing model size. While some change in coherence can be observed, it is minor especially in the frequency band of interest 3–10 Hz, where NN might limit the sensitivity of ET.

Finally, in plot (d),  $|c_{ij}(f)|$  is shown as a function of distance at frequency 5 Hz. The aforementioned qualitative difference between the flat surface and A3 topographic models can be seen again. The flat surface model closely follows the analytical model of an isotropic, flat surface Rayleigh wave field.

### 7.3. Gravity Displacement Correlation

It is possible to express the gravity perturbation produced by a seismic field in terms of an integral over seismic correlations (Harms, 2019). It is possible to separate contributions from compression and decompression of the ground medium by seismic waves and from surface displacement. Surface displacement is typically much stronger than underground displacement due to the presence of surface waves such as Rayleigh

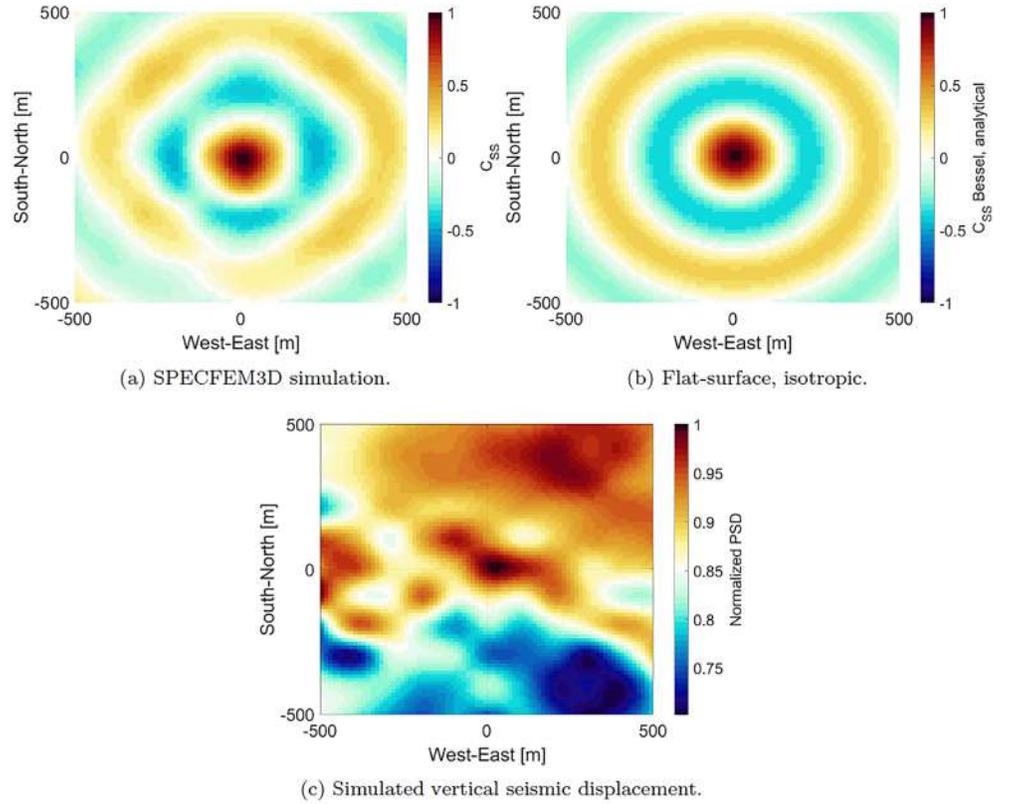


**Figure 12.** Normalized correlations (a) and spectral densities (c) calculated for an ambient field with SPEC-FEM3D at 5 Hz. The ideal (normalized) seismic correlations in the case of a flat surface and isotropic field is shown in (b).

waves. One of the reasons why ET is proposed as underground infrastructure is to avoid the relatively strong gravitational noise from surface displacement (Amann et al., 2020).

As a consequence, and as a first step, we attempt to model the gravitational coupling between seismic surface fields and underground gravitational perturbations. The equation to be used takes the form of a surface integral (Harms, 2019)

$$C(\delta a_{\text{arm}}(\mathbf{r}_0), \xi_z(\mathbf{r}); f) = G\rho_0 \int d^2\mathbf{r}' C(\xi_n(\mathbf{r}'), \xi_z(\mathbf{r}'); f) \frac{(\mathbf{r}' - \mathbf{r}_0) \cdot \mathbf{e}_{\text{arm}}}{|\mathbf{r}' - \mathbf{r}_0|^3}, \quad (13)$$

which is the CPSD between vertical seismic displacement  $\xi_z$  monitored at  $\mathbf{r}$  and horizontal gravitational acceleration  $\delta a_{\text{arm}}$  at the location  $\mathbf{r}_0$  of an underground TM. Here,  $G$  is Newton's gravitational constant,  $\rho_0$  is the mass density of a homogeneous ground, and  $\mathbf{e}_{\text{arm}}$  is the unit vector pointing along the detector arm of ET. The integral contains the CPSD between vertical and normal surface displacement provided by SPEC-FEM3D simulations. We focus on normal surface displacement typically associated with Rayleigh waves since lateral surface displacement does not produce gravity perturbations. This also explains why in this study we are not interested in contributions from Love waves, which can only generate gravity perturbations by displacement of underground cavern walls of the detector. In any case, our homogeneous model does not support the simulation of Love waves. Since a homogeneous medium is simulated here, Love waves do not play a role, but it is still convenient for practical reasons (when comparing with other work or seismic observations) to focus on vertical displacement.

The seismic CPSD  $C(\xi_n(\mathbf{r}' = \mathbf{0}), \xi_z(\mathbf{r}); f)$  for the A3 topographic model is shown in plot (a) of Figure 12. It only represents a small subset of all seismic correlations required for Equation 13. The result can be compared with the seismic CPSD in the case of a flat surface, isotropic Rayleigh wave field shown in plot (b). Topography has a significant impact on seismic correlations, but the pattern of concentric rings is approximately preserved. The third plot shows the variation of power spectral densities of vertical surface displacement. Again, topography leaves a clear imprint on the seismic field in the form of an inhomogeneity.

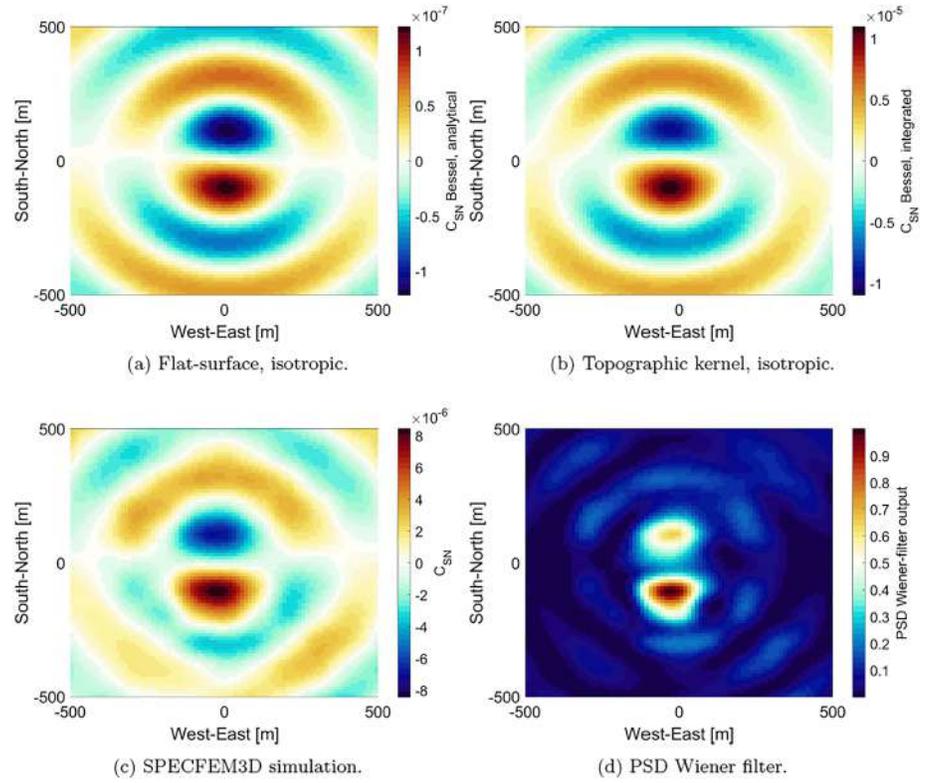


**Figure 13.** Seismic-gravitational correlations of an ambient field at 5 Hz (a)–(c) in arbitrary but consistent units. The normalized PSD of the Wiener-filter output is shown in (d). The test mass is located 100 m underground. The direction of gravity acceleration is along the A3–A1 detector arm.

Equation 13 can be solved analytically in the case of a flat surface, isotropic Rayleigh field, which yields (Harms, 2019):

$$C(\delta a_{\text{arm}}(\mathbf{0}), \xi_z(\mathbf{r}); f) = 2\pi G\rho_0 S(\xi_z; f) e^{-hk(f)} \cos(\phi) J_1(k(f)r), \quad (14)$$

with  $\mathbf{r} = (r \cos(\phi), r \sin(\phi), h)$ ,  $\phi$  being the angle between detector arm and the horizontal projection of  $\mathbf{r}$ , and  $k(f)$  is the wavenumber of plane Rayleigh waves. According to this model, the CPSD between vertical displacement and gravity perturbation vanishes for  $\mathbf{r} = \mathbf{0}$ . It is shown in plot (a) of Figure 13. Instead, plot (b) is calculated by inserting the isotropic, flat surface correlation of Equation 12 into Equation 13 but with a kernel that depends on topography. This shows that the kernel has an important impact on the seismic gravitational CPSD; for example, the nodal line along the south-north direction seen in plot (a) is not present in plot (b). Finally, the seismic gravitational CPSD calculated with the seismic CPSD from SPECIFEM3D and topographic kernel in Equation 13 is shown in plot (c).

The result in plot (d) tells us where a single seismometer should be placed to obtain the best reduction of NN by coherent cancelation with a Wiener filter. The plotted quantity is

$$S(w; f) = |C(\delta a_{\text{arm}}(\mathbf{r}_0), \xi_z(\mathbf{r}); f)|^2 / C(\xi_z(\mathbf{r}), \xi_z(\mathbf{r}); f), \quad (15)$$

which is the power spectral density of the output of the Wiener filter (Cella, 2000; Harms, 2019). The higher it is, the more NN the Wiener filter is able to cancel in the data of the ET. This optimal placement of a seismometer is at  $(-38, -113)$  m. The problem gets significantly more complicated if one wants to deploy multiple seismometers since the placement of sensors also depends on their mutual CPSDs (Badaracco & Harms, 2019). Nonetheless, the quantities required for such a multisensor optimization are provided by SPECIFEM3D. They need to be used in numerical optimization routines. What we in fact propose is to use the correlation results from numerical analysis as presented in this paper to define priors for a Gaussian Process Regression, which then combines priors and observed seismic correlations for a Bayesian inference of seismic correlations everywhere in the medium, which forms the basis of the optimization algorithm (Badaracco et al., 2020).

## 8. Conclusion

In this paper, we presented synthetic seismic and gravitoelastic correlations between seismometers and a suspended underground TM as part of the next generation, GW detector ET. The synthetics were calculated with the spectral element SPECFEM3D Cartesian software. The main analysis was based on a topographic model centered at one of the vertices (A3) at a candidate site in Sardinia of the ET.

We found that A3 topography has generally a significant impact on seismic and gravitoelastic correlations. Specifically, calculations showed that Sardinian topography at Vertex A3 scatters out energy from Rayleigh waves above 4 Hz providing protection from the influence of distant seismic sources. As expected, symmetries of the field of gravitoelastic correlations are broken by topography leading to unique solutions of optimal seismometer placement for gravity noise cancellation.

The results are a powerful demonstration of SPECFEM3D's capability to model correlations in ambient seismic fields for the purpose of designing noise cancellation systems using seismometer arrays. We proposed to use the numerical results to define priors of a Gaussian Process Regression, which includes seismic observations to infer gravitoelastic correlations throughout the entire ground medium. This is a crucial step to calculate optimal array configurations for gravity noise cancellation, which we expect to require several tens to hundreds of seismometers deployed in boreholes around 12 of the TM of the ET.

Since this work only addressed gravity perturbations from seismic surface displacement, an important future task is to extend the analysis to gravity perturbations resulting from (de)compression of rock by seismic waves and from displacement of underground cavern walls. In addition, geological inhomogeneities may be significant, which means that they should also be included in future modeling. Current understanding of geology near the three vertex locations can be improved by drill core and geoseismic studies, which would help to build a more accurate model and to improve simulation results.

## Data Availability Statement

To prepare the topography data, one can get SRTM Digital Elevation Data for a region of interest at <http://srtm.csi.cgiar.org> website. Besides, this is a modeling and simulation paper. There is no data necessary to understand, evaluate, or replicate our results. It is all based on creating a model and running the simulations on it, which anyone can repeat in principle with the information in the paper.

## Acknowledgments

SPECFEM3D is maintained by the Computational Infrastructure for Geodynamics (<http://geodynamics.org>), which is funded by the National Science Foundation under Awards EAR-0949446 and EAR-1550901. The work was supported by the PRIN project Characterization of the Sos Enattos mine in Sardinia as the site for the Einstein Telescope GW observatory. We thank the Sardinia site study team for useful discussions and suggestions for this manuscript. We acknowledge the usage of the high-performance cluster at CNAF, the central computing facility of INFN at Bologna. We are grateful for the continuous support we received from its staff.

## References

- Abbott, B. P., Abbott, R., Abbott, T. D., Abernathy, M. R., Acernese, F., Ackley, K., et al. (2016). GW150914: The advanced LIGO detectors in the era of first discoveries. *Physical Review Letters*, *116*, 131103. <https://doi.org/10.1103/PhysRevLett.116.131103>
- Abubakar, I. (1962). Scattering of plane elastic waves at rough surfaces. I. *Mathematical Proceedings of the Cambridge Philosophical Society*, *58*, 136–157. <https://doi.org/10.1017/S030500410003629X>
- Abubakar, I. (1963). Scattering of plane elastic waves at rough surfaces. II. *Mathematical Proceedings of the Cambridge Philosophical Society*, *59*, 231–248.
- Acernese, F., Agathos, M., Agatsuma, K., Aisa, D., Allemandou, N., Allocca, A., et al. (2015). Advanced Virgo: A second-generation interferometric gravitational wave detector. *Classical and Quantum Gravity*, *32*(2), 24001. <https://doi.org/10.1088/0264-9381/32/2/024001>
- Acernese, F., Antonucci, F., Aoudia, S., Arun, K. G., Astone, P., Ballardin, G., et al. (2010). Measurements of superattenuator seismic isolation by Virgo interferometer. *Astroparticle Physics*, *33*(3), 182–189. <https://doi.org/10.1016/j.astropartphys.2010.01.006>
- Adhikari, R. X., Arai, K., Brooks, A. F., Wipf, C., Aguiar, O., Altin, P., et al. (2020). A cryogenic silicon interferometer for gravitational-wave detection. *Classical and Quantum Gravity*, *37*(16), 165003. <https://doi.org/10.1088/1361-6382/ab9143>
- Aki, K., & Richards, P. G. (2009). *Quantitative seismology* (2nd ed.). Sausalito, USA: University Science Books.
- Akutsu, T., et al. (2019). KAGRA: 2.5 generation interferometric gravitational wave detector. *Nature Astronomy*, *3*(1), 35–40. <https://doi.org/10.1038/s41550-018-0658-y>
- Amann, F., Bonsignorio, F., Bulik, T., Bulten, H. J., Cuccuru, S., Dassargues, A., et al. (2020). Site-selection criteria for the Einstein Telescope. *Review of Scientific Instruments*, *91*(9), 094504. <https://doi.org/10.1063/5.0018414>
- Badaracco, F., & Harms, J. (2019). Optimization of seismometer arrays for the cancellation of Newtonian noise from seismic body waves. *Classical and Quantum Gravity*, *36*(14), 145006. <https://doi.org/10.1088/1361-6382/ab28c1>
- Badaracco, F., Harms, J., Bertolini, A., Bulik, T., Fiori, I., Idzkowski, B., et al. (2020). Machine learning for gravitational-wave detection: Surrogate Wiener filtering for the prediction and optimized cancellation of Newtonian noise at Virgo. *Classical and Quantum Gravity*, *37*(19), 195016. <https://doi.org/10.1088/1361-6382/abab64>
- Bard, P.-Y. (1982). Diffracted waves and displacement field over two-dimensional elevated topographies. *Geophysical Journal of the Royal Astronomical Society*, *71*(3), 731–760. <https://doi.org/10.1111/j.1365-246X.1982.tb02795.x>
- Barsotti, L., Harms, J., & Schnabel, R. (2019). Squeezed vacuum states of light for gravitational wave detectors. *Reports on Progress in Physics*, *82*(1), 16905. <https://doi.org/10.1088/1361-6633/aab906>
- Basini, P., Liu, Q., & Tape, C. (2012). Ambient-noise tomography of the Southern California lithosphere, *AGU fall meeting abstracts* (Vol. 2012, pp. S41A–2415). Washington DC, USA: American Geophysical Union.

- Basini, P., Nissen-Meyer, T., Boschi, L., Casarotti, E., Verbeke, J., Schenk, O., & Giardini, D. (2013). The influence of nonuniform ambient noise on crustal tomography in Europe. *Geochemistry, Geophysics, Geosystems*, *14*, 1471–1492. <https://doi.org/10.1002/ggge.20081>
- Beccaria, M., Bernardini, M., Braccini, S., Bradaschia, C., Bozzi, A., Casciano, C., et al. (1998). Relevance of Newtonian seismic noise for the VIRGO interferometer sensitivity. *Classical and Quantum Gravity*, *15*(11), 3339. Retrieved from <http://stacks.iop.org/0264-9381/15/i=11/a=004>
- Beker, M. G., Cella, G., DeSalvo, R., Doets, M., Grote, H., Harms, J., et al. (2011). Improving the sensitivity of future GW observatories in the 1–10 Hz band: Newtonian and seismic noise. *General Relativity and Gravitation*, *43*(2), 623–656. <https://doi.org/10.1007/s10714-010-1011-7>
- Beker, M. G., van den Brand, J. F. J., Hennes, E., & Rabeling, D. S. (2012). Newtonian noise and ambient ground motion for gravitational wave detectors. *Journal of Physics: Conference Series*, *363*(1), 12004. Retrieved from <http://stacks.iop.org/1742-6596/363/i=1/a=012004>
- Beker, M. G., van den Brand, J. F. J., & Rabeling, D. S. (2015). Subterranean ground motion studies for the Einstein Telescope. *Classical and Quantum Gravity*, *32*(2), 25002. Retrieved from <http://stacks.iop.org/0264-9381/32/i=2/a=025002>
- Blacker, T., Quadros, R. W., Owen, S. J., Staten, M. L., Hanks, B., Clark, B., et al. (2019). Trellis v16.5 [software].
- Bonnefoy-Claudet, S., Cotton, F., & Bard, P.-Y. (2006). The nature of noise wavefield and its applications for site effects studies: A literature review. *Earth-Science Reviews*, *79*(3–4), 205–227. <https://doi.org/10.1016/j.earscirev.2006.07.004>
- Cella, G. (2000). Off-line subtraction of seismic Newtonian noise. In B. Casciaro, D. Fortunato, M. Francaviglia, & A. Masiello (Eds.), *Recent developments in general relativity* (pp. 495–503). Milan, Italy: Springer. [https://doi.org/10.1007/978-88-470-2113-6\\_44](https://doi.org/10.1007/978-88-470-2113-6_44)
- Chan, M. L., Messenger, C., Heng, I. S., & Hendry, M. (2018). Binary neutron star mergers and third generation detectors: Localization and early warning. *Physical Review D*, *97*, 123014. <https://doi.org/10.1103/PhysRevD.97.123014>
- Coughlin, M., & Harms, J. (2012). Seismic topographic scattering in the context of GW detector site selection. *Classical and Quantum Gravity*, *29*, 75004. Retrieved from <http://stacks.iop.org/0264-9381/29/i=7/a=075004>
- Coughlin, M., Harms, J., Bowden, D. C., Meyers, P., Tsai, V. C., Mandic, V., et al. (2019). Coherence-based approaches for estimating the composition of the seismic wavefield. *Journal of Geophysical Research: Solid Earth*, *124*, 2941–2956. <https://doi.org/10.1029/2018JB016608>
- Coughlin, M. W., Harms, J., Driggers, J., McManus, D. J., Mukund, N., Ross, M. P., et al. (2018). Implications of dedicated seismometer measurements on Newtonian-noise cancellation for advanced LIGO. *Physical Review Letters*, *121*, 221104. <https://doi.org/10.1103/PhysRevLett.121.221104>
- Coughlin, M., Mukund, N., Harms, J., Driggers, J., Adhikari, R., & Mitra, S. (2016). Towards a first design of a Newtonian-noise cancellation system for advanced LIGO. *Classical and Quantum Gravity*, *33*(24), 244001. Retrieved from <http://stacks.iop.org/0264-9381/33/i=24/a=244001>
- Dahlen, F. A., & Tromp, J. (1998). *Theoretical global seismology* (944 pp.). Princeton, USA: Princeton University Press.
- Driggers, J. C., Harms, J., & Adhikari, R. X. (2012). Subtraction of Newtonian noise using optimized sensor arrays. *Physical Review D*, *86*, 102001. <https://doi.org/10.1103/PhysRevD.86.102001>
- ET Science Team (2011). Einstein gravitational wave Telescope conceptual design study. available from European Gravitational Observatory, document number ET-0106C-10.
- Fan, Y., & Snieder, R. (2009). Required source distribution for interferometry of waves and diffusive fields. *Geophysical Journal International*, *179*(2), 1232–1244. <https://doi.org/10.1111/j.1365-246X.2009.04358.x>
- Fiorucci, D., Harms, J., Barsuglia, M., Fiori, I., & Paoletti, F. (2018). Impact of infrasound atmospheric noise on gravity detectors used for astrophysical and geophysical applications. *Physical Review D*, *97*, 62003. <https://doi.org/10.1103/PhysRevD.97.062003>
- Gilbert, F., & Knopoff, L. (1960). Seismic scattering from topographic irregularities. *Journal of Geophysical Research*, *65*(10), 3437–3444. <https://doi.org/10.1029/JZ065i010p03437>
- Giunchi, C., Di Giovanni, M., Saccorotti, G., & Naticchioni, L. (2020). Seismic noise characterization of the Sos Enattos Mine (Sardinia), a candidate site for the next generation of terrestrial gravitational waves detectors. EGU General Assembly 2020, Online, EGU2020-9692 <https://doi.org/10.5194/egusphere-egu2020-9692>
- Grimm, S., & Harms, J. (2020). Multiband gravitational wave parameter estimation: A study of future detectors. *Physical Review D*, *102*(2). <https://doi.org/10.1103/physrevd.102.022007>
- Gropp, W., Lusk, E., & Skjellum, A. (1994). *Using MPI, portable parallel programming with the message-passing interface*. Cambridge, USA: MIT Press. <https://doi.org/10.7551/mitpress/7056.001.0001>
- Harms, J. (2019). Terrestrial gravity fluctuations. *Living Reviews in Relativity*, *22*(1), 6. <https://doi.org/10.1007/s41114-019-0022-2>
- Hanasoge, S., Stehly, L., Nissen-Meyer, T., & Cupillard, P. (2012). Non-linear iterative inversions for the distribution of noise sources, *AGU fall meeting abstracts* (Vol. 2012, pp. S53C–2513). Washington DC, USA: American Geophysical Union.
- Harms, J., Acernese, F., Barone, F., Bartos, I., Beker, M., van den Brand, J. F. J., et al. (2010). Characterization of the seismic environment at the Sanford Underground Laboratory, South Dakota. *Classical and Quantum Gravity*, *27*(22), 225011. Retrieved from <http://stacks.iop.org/0264-9381/27/i=22/a=225011>
- Harms, J., Bonilla, E. L., Coughlin, M. W., Driggers, J., Dwyer, S. E., McManus, D. J., et al. (2020). Observation of a potential future sensitivity limitation from ground motion at LIGO Hanford. *Physical Review D*, *101*, 102002. <https://doi.org/10.1103/PhysRevD.101.102002>
- Hild, S., Abernathy, M., Acernese, F., Amaro-Seoane, P., Andersson, N., Arun, K., et al. (2011). Sensitivity studies for third-generation gravitational wave observatories. *Classical and Quantum Gravity*, *28*(9), 94013. Retrieved from <http://stacks.iop.org/0264-9381/28/i=9/a=094013>
- Hild, S., Chelkowsky, S., Freise, A., Franc, J., Morgado, N., Flaminio, R., & DeSalvo, R. (2009). A xylophone configuration for a third-generation gravitational wave detector. *Classical and Quantum Gravity*, *27*(1), 15003. <https://doi.org/10.1088/0264-9381/27/1/015003>
- Hudson, J. A. (1967). Scattered surface waves from a surface obstacle. *Geophysical Journal International*, *13*(4), 441–458. <https://doi.org/10.1111/j.1365-246X.1967.tb03143.x>
- Hudson, J. A., Humphryes, R. F., Mason, I. M., & Kembhavi, V. K. (1973). The scattering of longitudinal elastic waves at a rough free surface. *Journal of Physics D Applied Physics*, *6*(18), 2174–2186. <https://doi.org/10.1088/0022-3727/6/18/303>
- Hudson, J. A., & Knopoff, L. (1967). Statistical properties of Rayleigh waves due to scattering by topography. *Bulletin of the Seismological Society of America*, *57*, 83–90.
- Hughes, S. A., & Thorne, K. S. (1998). Seismic gravity-gradient noise in interferometric gravitational-wave detectors. *Physical Review D*, *58*, 122002. <https://doi.org/10.1103/PhysRevD.58.122002>
- Komatitsch, D. (2004). Simulations of ground motion in the Los Angeles basin based upon the spectral-element method. *The Bulletin of the Seismological Society of America*, *94*(1), 187–206. <https://doi.org/10.1785/0120030077>

- Komatitsch, D., Labarta, J., & Michéa, D. (2008). A simulation of seismic wave propagation at high resolution in the inner core of the Earth on 2166 processors of MareNostrum. *Lecture Notes in Computer Science*, 5336, 364–377. [https://doi.org/10.1007/978-3-540-92859-1\\_33](https://doi.org/10.1007/978-3-540-92859-1_33)
- Komatitsch, D., & Martin, R. (2007). An unsplit convolutional perfectly matched layer improved at grazing incidence for the seismic wave equation. *Geophysics*, 72(5), SM155. <https://doi.org/10.1190/1.2757586>
- Komatitsch, D., & Tromp, J. (1999). Introduction to the spectral element method for three-dimensional seismic wave propagation. *Geophysical Journal International*, 139(3), 806–822. <https://doi.org/10.1046/j.1365-246x.1999.00967.x>
- Komatitsch, D., & Tromp, J. (2002a). Spectral-element simulations of global seismic wave propagation I. Validation. *Geophysical Journal International*, 149(2), 390–412. <https://doi.org/10.1046/j.1365-246X.2002.01653.x>
- Komatitsch, D., & Tromp, J. (2002b). Spectral-element simulations of global seismic wave propagation-II. Three-dimensional models, oceans, rotation and self-gravitation. *Geophysical Journal International*, 150(1), 303–318. <https://doi.org/10.1046/j.1365-246X.2002.01716.x>
- Komatitsch, D., Tsuboi, S., Ji, C., & Tromp, J. (2003). A 14.6 billion degrees of freedom, 5 teraflops, 2.5 terabyte earthquake simulation on the Earth simulator, *Proceedings of the SC'03 ACM/IEEE conference on supercomputing* (pp. 4–11). Phoenix, Arizona, USA: ACM. (Gordon Bell Prize winner article) <https://doi.org/10.1145/1048935.1050155>
- Komatitsch, D., & Vilotte, J.-P. (1998). The spectral element method: An efficient tool to simulate the seismic response of 2D and 3D geological structures. *Bulletin of the Seismological Society of America*, 88(2), 368–392. Retrieved from <http://www.bssaonline.org/content/88/2/368.abstract>
- Komatitsch, D., Vilotte, J.-P., Afanasiev, M., Ampuero, J.-P., Bachmann, E., Bai, K., et al. (2018). SPECFEM3D Cartesian v3.0 [software].
- Komatitsch, D., Vilotte, J.-P., Vai, R., Castillo-Covarrubias, J. M., & Sánchez-Sesma, F. J. (1999). The spectral element method for elastic wave equations—application to 2-D and 3-D seismic problems. *International Journal for Numerical Methods in Engineering*, 45(9), 1139–1164. [https://doi.org/10.1002/\(SICI\)1097-0207\(19990730\)45:9<1139::AID-NME617i3.0.CO;2-T](https://doi.org/10.1002/(SICI)1097-0207(19990730)45:9<1139::AID-NME617i3.0.CO;2-T)
- Liu, Q., & Tromp, J. (2006). Finite-frequency kernels based on adjoint methods. *The Bulletin of the Seismological Society of America*, 96(6), 2383–2397. <https://doi.org/10.1785/0120060041>
- Liu, Q., & Tromp, J. (2008). Finite-frequency sensitivity kernels for global seismic wave propagation based upon adjoint methods. *Geophysical Journal International*, 174(1), 265–286. <https://doi.org/10.1111/j.1365-246X.2008.03798.x>
- Lobkis, O. I., & Weaver, R. L. (2001). On the emergence of the Green's function in the correlations of a diffuse field. *The Journal of the Acoustical Society of America*, 110(6), 3011–3017. <https://doi.org/10.1121/1.1417528>
- Maday, Y., & Patera, A. T. (1989). Spectral element methods for the incompressible Navier-Stokes equations, In: *State-of-the-art surveys on computational mechanics (a90-47176 21-64)* (Vol. 1, pp. 71–143). New York, USA: American Society of Mechanical Engineers.
- Maggiore, M., Broeck, C. V. D., Bartolo, N., Belgacem, E., Bertacca, D., Bizouard, M. A., et al. (2020). Science case for the Einstein telescope. *Journal of Cosmology and Astroparticle Physics*, 2020(03), 50. <https://doi.org/10.1088/1475-7516/2020/03/050>
- Mandic, V., Tsai, V. C., Pavlis, G. L., Prestegard, T., Bowden, D. C., Meyers, P., & Caton, R. (2018). A 3D broadband seismometer array experiment at the Homestake Mine. *Seismological Research Letters*, 89(6), 2420. <https://doi.org/10.1785/0220170228>
- Maradudin, A., & Mills, D. L. (1976). Attenuation of Rayleigh surface waves by surface roughness. *Annals of Physics*, 100, 262–309. [https://doi.org/10.1016/0003-4916\(76\)90063-4](https://doi.org/10.1016/0003-4916(76)90063-4)
- Martin, R., & Komatitsch, D. (2009). An unsplit convolutional perfectly matched layer technique improved at grazing incidence for the viscoelastic wave equation. *Geophysical Journal International*, 179(1), 333–344. <https://doi.org/10.1111/j.1365-246X.2009.04278.x>
- Martin, R., Komatitsch, D., Gedney, S., & Bruthiaux, E. (2010). A high-order time and space formulation of the unsplit perfectly matched layer for the seismic wave equation using auxiliary differential equations (ade-pml). *Computer Modelling in Engineering and Sciences - CMES*, 56, 17–42. <https://doi.org/10.3970/cmescs.2010.056.017>
- Matichard, F., Lantz, B., Mason, K., Mittleman, R., Abbott, B., Abbott, S., et al. (2014). Advanced LIGO two-stage twelve-axis vibration isolation and positioning platform. Part I: Design and production overview. *Precision Engineering*, 40, 273–286. <https://doi.org/10.1016/j.precisioneng.2014.09.010>
- Montagner, J.-P., Larmat, C., Capdeville, Y., Fink, M., Phung, H., Romanowicz, B., et al. (2012). Time-reversal method and cross-correlation techniques by normal mode theory: A three-point problem. *Geophysical Journal International*, 191(2), 637–652. <https://doi.org/10.1111/j.1365-246X.2012.05619.x>
- Mooney, H. M. (1976). The seismic wave system from a surface impact. *Geophysics*, 41(2), 243–265. <https://doi.org/10.1190/1.1440614>
- Ogilvy, J. A. (1987). Wave scattering from rough surfaces. *Reports on Progress in Physics*, 50(12), 1553. <https://doi.org/10.1088/0034-4885/50/12/001>
- Olsen, K. B., Madariaga, R., & Archuleta, R. J. (1997). Three-dimensional dynamic simulation of the 1992 Landers earthquake. *Science*, 278, 834–838. <https://doi.org/10.1126/science.278.5339.834>
- Orfanidis, S. J. (2007). *Optimum signal processing: An introduction*. New York City, USA: Macmillan Publishing Company.
- Otto, O. W. (1977). Scattering of Rayleigh waves from topographic irregularities at oblique incidence. *Journal of Applied Physics*, 48(12), 5105–5110. <https://doi.org/10.1063/1.323587>
- Pacheco, P. S. (1997). *Parallel programming with MPI*. San Francisco, USA: Morgan Kaufmann Press.
- Patera, A. T. (1984). A spectral element method for fluid dynamics: Laminar flow in a channel expansion. *Journal of Computational Physics*, 54(3), 468–488. [https://doi.org/10.1016/0021-9991\(84\)90128-1](https://doi.org/10.1016/0021-9991(84)90128-1)
- Peter, D., Komatitsch, D., Luo, Y., Martin, R., Le Goff, N., Casarotti, E., et al. (2011). Forward and adjoint simulations of seismic wave propagation on fully unstructured hexahedral meshes. *Geophysical Journal International*, 186(2), 721–739. <https://doi.org/10.1111/j.1365-246X.2011.05044.x>
- Peter, D., Tape, C., Boschi, L., & Woodhouse, J. H. (2007). Surface wave tomography: Global membrane waves and adjoint methods. *Geophysical Journal International*, 171(3), 1098–1117. <https://doi.org/10.1111/j.1365-246X.2007.03554.x>
- Punturo, M., Abernathy, M., Acernese, F., Allen, B., Andersson, N., Arun, K., et al. (2010). The Einstein telescope: A third-generation gravitational wave observatory. *Classical and Quantum Gravity*, 27(19), 194002. Retrieved from <http://stacks.iop.org/0264-9381/27/i=19/a=194002>
- Reitze, D., Adhikari, R. X., Ballmer, S., Barish, B., Barsotti, L., Billingsley, G., et al. (2019). Cosmic explorer: The U.S. contribution to gravitational-wave astronomy beyond LIGO. *Bulletin of the American Astronomical Society*, 51, 035.
- Sanchez-Sesma, F. J., & Campillo, M. (1991). Diffraction of P, SV and Rayleigh waves by topographic features: A boundary integral formulation. *Bulletin - Seismological Society of America*, 81(6), 2234–2253.
- Sathyaprakash, B., Abernathy, M., Acernese, F., Ajith, P., Allen, B., Amaro-Seoane, P., et al. (2012). Scientific objectives of Einstein telescope. *Classical and Quantum Gravity*, 29(12), 124013. Retrieved from <http://stacks.iop.org/0264-9381/29/i=12/a=124013>
- Seriani, G., & Priolo, E. (2012). Spectral element method for acoustic wave simulation in heterogeneous media. *Finite Elements in Analysis and Design*, 16, 337–348. [https://doi.org/10.1016/0168-874X\(94\)90076-0](https://doi.org/10.1016/0168-874X(94)90076-0)

- Snieder, R. (1986). The influence of topography on the propagation and scattering of surface waves. *Physics of the Earth and Planetary Interiors*, 44(3), 226–241. [https://doi.org/10.1016/0031-9201\(86\)90072-5](https://doi.org/10.1016/0031-9201(86)90072-5)
- Souradeep, T. (2016). LIGO-India. *Resonance*, 21, 225–231. <https://doi.org/10.1007/s12045-016-0316-6>
- Tromp, J., Komatitsch, D., & Liu, Q. (2008). Spectral-element and adjoint methods in seismology. *Communications in Computational Physics*, 3(1), 1–32.
- Tromp, J., Luo, Y., Hanasoge, S., & Peter, D. (2010). Noise cross-correlation sensitivity kernels. *Geophysical Journal International*, 183(2), 791–819. <https://doi.org/10.1111/j.1365-246X.2010.04721.x>
- Tromp, J., Tape, C., & Liu, Q. (2005). Seismic tomography, adjoint methods, time reversal and banana-doughnut kernels. *Geophysical Journal International*, 160(1), 195–216. <https://doi.org/10.1111/j.1365-246X.2004.02453.x>
- Tsai, V. C., & Moschetti, M. P. (2010). An explicit relationship between time-domain noise correlation and spatial autocorrelation (SPAC) results. *Geophysical Journal International*, 182(1), 454–460. <https://doi.org/10.1111/j.1365-246X.2010.04633.x>
- Tsuboi, S., Komatitsch, D., Ji, C., & Tromp, J. (2003). Broadband modeling of the 2002 Denali fault earthquake on the Earth simulator. *Physics of the Earth and Planetary Interiors*, 139(3–4), 305–313. <https://doi.org/10.1016/j.pepi.2003.09.012>
- Virieux, J. (1986). P-SV wave propagation in heterogeneous media: Velocity-stress finite-difference method. *Geophysics*, 51(4), 889–901. <https://doi.org/10.1190/1.1442147>
- Wapenaar, K., Slob, E., & Snieder, R. (2006). Unified Green's function retrieval by cross correlation. *Physical Review Letters*, 97(23), 234301. <https://doi.org/10.1103/PhysRevLett.97.234301>
- Woodard, M. F. (1997). Implications of localized, acoustic absorption for heliotomographic analysis of sunspots. *The Astrophysical Journal*, 485(2), 890–894. <https://doi.org/10.1086/304468>
- Woods, R. D. (1968). Screening of surface waves in soils. *Journal of the Soil Mechanics and Foundations Division: proceedings of the American Society of Civil Engineers*, 94(4), 951–979.
- Xie, Z., Komatitsch, D., Martin, R., & Matzen, R. (2014). Improved forward wave propagation and adjoint-based sensitivity kernel calculations using a numerically stable finite-element PML. *Geophysical Journal International*, 198(3), 1714–1747. <https://doi.org/10.1093/gji/ggu219>